

1

2 The ANTsX Ecosystem for Spatiotemporal 3 Mapping of the Mouse Brain

4 Nicholas J. Tustison¹, Min Chen², Fae N. Kronman³, Jeffrey T. Duda², Clare Gamlin⁴,
5 Lydia Ng⁴, Yongsoo Kim³, and James C. Gee²

6 ¹Department of Radiology and Medical Imaging, University of Virginia, Charlottesville, VA

7 ²Department of Radiology, University of Pennsylvania, Philadelphia, PA

8 ³Department of Neural and Behavioral Sciences, Penn State University, Hershey, PA

9 ⁴Allen Institute for Brain Science, Seattle, WA

10

11 Corresponding author:

12 Nicholas J. Tustison, DSc

13 Department of Radiology and Medical Imaging

14 University of Virginia

15 ntustison@virginia.edu

₁₆ **Abstract**

₁₇ Precision mapping techniques coupled with high resolution image acquisition of the mouse
₁₈ brain permit the study of the spatial organization of gene activity and their mutual interac-
₁₉ tion for a comprehensive view of salient structural/functional relationships. Such research
₂₀ is facilitated by standardized anatomical coordinate systems, such as the well-known Allen
₂₁ Common Coordinate Framework version 3 (CCFv3), and the ability to map to such refer-
₂₂ ence atlases. The Advanced Normalization Tools Ecosystem (ANTsX) is a comprehensive
₂₃ open-source software image analysis toolkit with applicability to multiple organ systems,
₂₄ modalities, and animal species. Herein, we illustrate the utility of ANTsX for generating
₂₅ precision spatial mappings of the mouse brain of different developmental ages including the
₂₆ prerequisite preprocessing steps. Additionally, as a further illustration of ANTsX capabil-
₂₇ ities, we use these publicly available mouse brain atlases to generate a velocity flow-based
₂₈ mapping encompassing the entire developmental trajectory, which we also make available to
₂₉ the public.

³⁰ Introduction

³¹ Over the past two decades there has been a notable increase in significant advancements in
³² mesoscopic analysis of the mouse brain. It is now possible to track single cell neurons in 3-D
³³ across full mouse brains,¹ observe whole brain developmental changes on a cellular level,²
³⁴ associate brain regions and tissues with their genetic composition,³ and locally characterize
³⁵ neural connectivity.⁴ Much of this scientific achievement has been made possible due to
³⁶ breakthroughs in high resolution imaging techniques that permit submicron, 3-D imaging
³⁷ of whole mouse brains. Associated research techniques such as micro-optical sectioning
³⁸ tomography,⁶ tissue clearing,^{1,7} spatial transcriptomics⁹ are all well-utilized in the course of
³⁹ scientific investigations of mesoscale relationships in the mouse brain.

⁴⁰ An important component of these research programs is the ability to map the various image
⁴¹ data to anatomical reference frames¹¹ for inferring spatial relationships between structures,
⁴² cells, and genetics in the brain. This has motivated the development of detailed struc-
⁴³ tural image atlases of the mouse brain. Notable examples include the Allen Brain Atlas
⁴⁴ and Coordinate Frameworks¹³ and the Waxholm Space.¹⁴ Despite the significance of these
⁴⁵ contributions, challenges still exist in large part due to the wide heterogeneity in associ-
⁴⁶ ated study-specific image data. Variance in the acquisition methods can introduce artifacts
⁴⁷ such as tissue distortion, holes, bubbles, folding, tears, and missing slices. These severely
⁴⁸ complicate assumed correspondence for registration.

⁴⁹ To address such challenges, several software packages have been developed over the years
⁵⁰ comprising solutions of varying comprehensibility, sophistication, and availability. An early
⁵¹ contribution to the community was the Rapid Automatic Tissue Segmentation (RATS)
⁵² package¹⁵ for brain extraction (available upon request). Of the publicly available pack-
⁵³ ages, most, if not all rely on well-established package dependencies originally developed on
⁵⁴ human brain data. Another early tool was SPMMouse¹⁶ based on the well-known Statistical
⁵⁵ Parametric Mapping (SPM) software package.¹⁷ The automated mouse atlas propagation
⁵⁶ (aMAP) tool is largely a front-end for the NiftyReg image registration package¹⁸ applied
⁵⁷ to mouse data which is currently available as a Python module.¹⁹ NiftyReg is also used by
⁵⁸ the Atlas-based Imaging Data Analysis (AIDA) MRI pipeline²⁰ as well as the Multi Atlas

59 Segmentation and Morphometric Analysis Toolkit (MASMAT). Whereas the former also in-
60 corporates the FMRIB Software Library (FSL)²¹ for brain extraction and DSISTudio²² for
61 DTI processing, the latter uses NiftySeg and multi-consensus labeling tools²³ for brain extrac-
62 tion and parcellation. In addition, MASMAT incorporates N4 bias field correction²⁴ from the
63 Advanced Normalization Tools Ecosystem (ANTsX)²⁵ as do the packages Multi-modal Image
64 Registration And Connectivity anaLysis (MIRACL),²⁶ Saamba-MRI,²⁷ and Small Animal
65 Magnetic Resonance Imaging (SAMRI).²⁸ However, whereas Saamba-MRI uses AFNI²⁹ for
66 image registration; MIRACL, SAMRI, and BrainsMap³⁰ all use ANTsX tools for comput-
67 ing image-based correspondences. Other packages use landmark-based approaches to image
68 registration including SMART—³¹an R package for semi-automated landmark-based regis-
69 tration and segmentation of mouse brain based on WholeBrain.³² FriendlyClearMap³³ uses
70 the landmark-based registration functionality of Elastix.³⁴ Finally, the widespread adop-
71 tion of deep learning techniques has also influenced development in mouse brain imaging
72 methodologies. For example, if tissue deformations are not considered problematic for a
73 particular dataset, DeepSlice can be used to determine affine mappings³⁵ with the optimal
74 computational efficiency associated with neural networks.

75 The ANTsX Ecosystem

76 As noted above, many of the existing approaches for processing of mouse brain image data
77 use ANTsX tools for core steps in various workflows, particularly its pairwise, intensity-
78 based image registration tools and bias field correction. Historically, ANTsX development
79 is originally based on fundamental approaches to image mapping,^{36–38} particularly in the
80 human brain, which has resulted in core contributions to the field such as the well-known and
81 highly-vetted Symmetric Normalization (SyN) algorithm.³⁹ Since its development, various
82 independent platforms have been used to evaluate ANTsX image registration capabilities in
83 the context of different application foci which include multi-site brain MRI data,⁴⁰ pulmonary
84 CT data,⁴¹ and most recently multi-modal brain registration in the presence of tumors.⁴²
85 Apart from its registration capabilities, ANTsX is a comprehensive biological and medical
86 image analysis toolkit, that comprises additional functionality such as template generation,

Table 1: Sampling of ANTsX functionality

<i>ANTsPy: Preprocessing</i>	
bias field correction	<code>n4_bias_field_correction(...)</code>
image denoising	<code>denoise_image(...)</code>
<i>ANTsPy: Registration</i>	
image registration	<code>registration(...)</code>
template generation	<code>build_template(...)</code>
landmark registration	<code>fit_transform_to_paired_points(...)</code>
time-varying landmark reg.	<code>fit_time_varying_transform_to_point_sets(...)</code>
integrate velocity field	<code>integrate_velocity_field(...)</code>
invert displacement field	<code>invert_displacement_field(...)</code>
<i>ANTsPy: Segmentation</i>	
General segmentation	<code>atropos(...)</code>
Joint label fusion	<code>joint_label_fusion(...)</code>
diffeomorphic thickness	<code>kelly_kapowski(...)</code>
<i>ANTsPy: Miscellaneous</i>	
Regional intensity statistics	<code>label_stats(...)</code>
Regional shape measures	<code>label_geometry_measures(...)</code>
B-spline approximation	<code>fit_bspline_object_to_scattered_data(...)</code>
Visualize images and overlays	<code>plot(...)</code>
<i>ANTsPyNet</i>	
brain extraction	<code>mouse_brain_extraction(...modality="t2"...)</code> <code>mouse_brain_extraction(...modality="ex5"...)</code>
foreground extraction	<code>mouse_histology_brain_mask(...)</code>
midline segmentation	<code>mouse_histology_hemispherical_coronal_mask(...)</code>
cerebellum segmentation	<code>mouse_histology_cerebellum_mask(...)</code>
super resolution	<code>mouse_histology_super_resolution(...)</code>

ANTsX provides state-of-the-art open-science functionality for processing image data. Such tools, including deep learning networks, support a variety of mapping-related tasks. A more comprehensive listing of ANTsX tools with self-contained R and Python examples is provided as a gist page on GitHub (<https://tinyurl.com/antsxtutorial>).

general data approximation, and deep learning networks specifically trained for mouse data (see Table 1). The collective use of the toolkit has demonstrated superb performance in multiple application areas (e.g., consensus labeling,⁴³ brain tumor segmentation,⁴⁴ and cardiac motion estimation).⁴⁵ Importantly, ANTs is built on the Insight Toolkit (ITK)⁴⁶ deriving benefit from a very capable open-source community of scientists and programmers as well as providing a visible, open-source venue for algorithmic contributions.

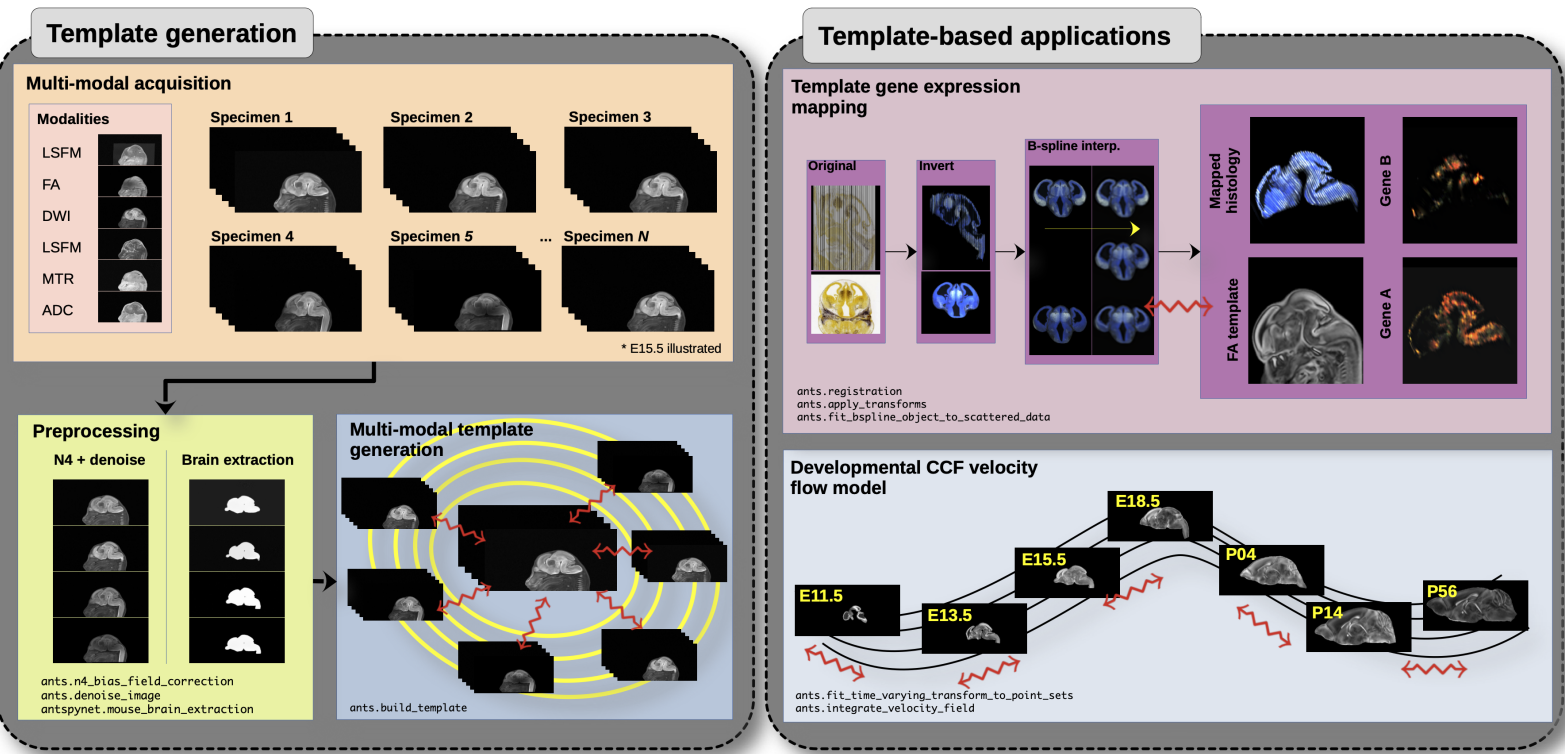


Figure 1: Illustration of a mouse brain template generation workflow and related template-based applications demonstrating the utility of different ANTsX tools. After imaging acquisition of the study population, various preprocessing steps are applied to the imaging data such as bias correction, denoising, and brain extraction as dictated by the needs of the study protocol. Not shown is the possibility of template symmetrization by contralaterally flipping the image data associated with each specimen. In the case of the DevCCF, applications include gene expression mapping and the associated velocity flow model for pseudo-template generation.

Recently, the developmental common coordinate framework (DevCCF) was introduced to the mouse brain research community as a public resource.⁴⁷ These symmetric atlases, comprising both multimodal image data and anatomical segmentations defined by developmental

96 ontology, span the mouse embryonic days (E) 11.5, E13.5, E15.5, E18.5 and postnatal day
97 (P) 4, P14, and P56. Modalities include at least four MRI contrasts and light sheet flores-
98 cence microscopy (LSFM) per developmental stage. Gene expression and other cell type
99 data were mapped to the corresponding developmental time point to guide the associated
100 anatomical parcellations. To further demonstrate the practical utility of the DevCCF, the
101 P56 template was integrated with the Allen CCFv3 for mapping spatial transcriptome cell-
102 type data. These processes, specifically template generation and multi-modal image map-
103 ping, were performed using ANTsX functionality in the presence of previously noted image
104 mapping difficulties (e.g., missing slices, tissue distortion) illustrated in Figure 1.

105 Given the temporal gaps in the discrete set of developmental atlases, we augment the tem-
106 plate generation explanation previously given⁴⁷ from a developer’s perspective. We hope that
107 this will provide additional information for the interested reader for potential future template
108 generation. Related, we also provide a complementary strategy for inferring correspondence
109 and mapping information within the temporally continuous domain spanned and sampled by
110 the existing set of embryonic and postnatal atlas brains of the DevCCF. Recently developed
111 ANTsX functionality include the generation of a diffeomorphic velocity flow transformation
112 model⁴⁸ spanning developmental stages where mappings between any two continuous time
113 points within the span bounded by the E11.5 and P56 atlases is determined by integration
114 of the generated time-varying velocity field.⁴⁹ Such transformations permit the possibility of
115 “pseudo” templates generated between available developmental stages.

₁₁₆ **Results**

₁₁₇ **Template building**

₁₁₈ Template building using ANTsX tools was first described in.⁵⁰ Subsequently, multi-modal and
₁₁₉ symmetrical variants were more explicitly described as part of the brain tumor segmentation
₁₂₀ approach.⁵¹

₁₂₁ **The DevCCF Velocity Flow Model**

₁₂₂ To continuously link the DevCCF atlases, a velocity flow model was constructed using Dev-
₁₂₃ CCF derived data and ANTsX functionality available in both ANTsR and ANTsPy. Al-
₁₂₄ though many implementations optimize variations of this transformation model (and others)
₁₂₅ using various image intensity similarity metrics, we opted to implement a separate de-
₁₂₆ termination of iterative correspondence and transformation optimization. This decision was
₁₂₇ based on existing ANTsX functionality and wanting complementary utility for the toolkit.

₁₂₈ ANTsX, being built on top of ITK, uses an ITK image data structure for the 4-D velocity
₁₂₉ field where each voxel contains the x , y , z components of the field at that point. Field
₁₃₀ regularization is provided by a novel B-spline scattered data approximation technique⁵² which
₁₃₁ permits individual point-based weighting. Both field regularization and integration of the
₁₃₂ velocity field are built on ITK functions written by ANTsX developers.

₁₃₃ The optimized velocity field described here is of size [256, 182, 360] (or $50\mu\text{m}$ isotropic) $\times 11$
₁₃₄ integration points for a total compressed size of a little over 2 GB. This choice represented
₁₃₅ weighing the trade-off between tractability, portability, and accuracy. However, all data
₁₃₆ and code to reproduce the results described are available in a dedicated GitHub repository
₁₃₇ (<https://github.com/ntustison/DevCCF-Velocity-Flow>).

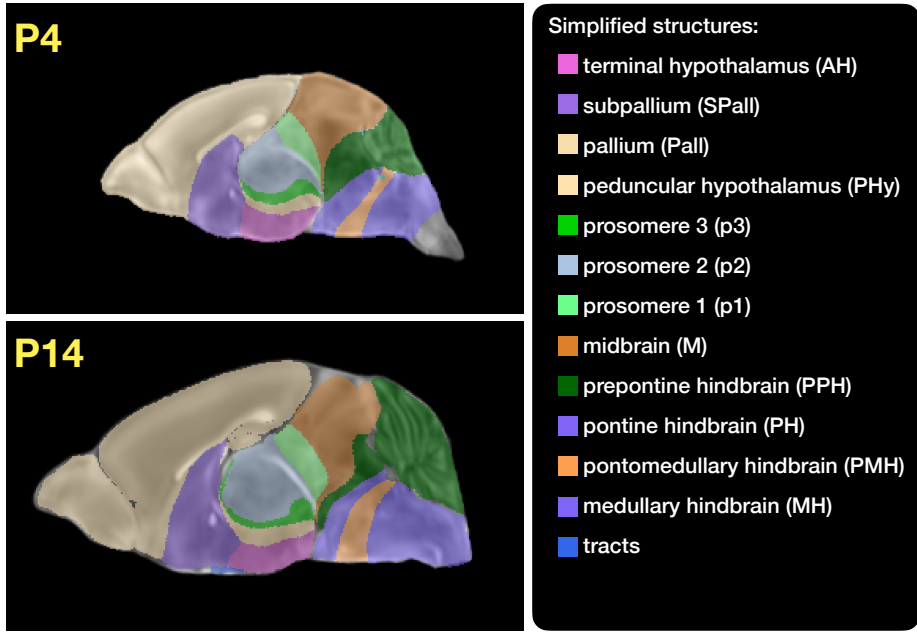


Figure 2: Annotated regions representing common labels across developmental stages which are illustrated for both P4 and P14.

¹³⁸ Data preparation

¹³⁹ Labeled annotations are available as part of the original DevCCF and reside in the space
¹⁴⁰ of each developmental template which range in resolution from $31.5 - 50\mu\text{m}$. Across all atlases,
¹⁴¹ the total number of labels exceeded 2500 without taken into account per hemispherical
¹⁴² enumeration. From this set of labels, there were a common set of 24 labels (12 per hemisphere)
¹⁴³ across all atlases that were used for optimization and evaluation. These regions are
¹⁴⁴ illustrated for the P4 and P14 stages in Figure 2.

¹⁴⁵ Prior to velocity field optimization, the data was rigidly transformed to a common
¹⁴⁶ space. Using the centroids for the common label set of each CCFDev atlas, the ANTsPy
¹⁴⁷ `ants.fit_transform_to_paired_points(...)` function was used to warp each atlas
¹⁴⁸ to the space of the P56 atlas and then downsampled to $50\mu\text{m}$ isotropic resolution. In
¹⁴⁹ order to determine the common point sets across stages, `ants.registration(...)` and
¹⁵⁰ its multi-metric capabilities were used. Instead of performing intensity-based registration
¹⁵¹ directly on these multi-label images, each label was used to construct a separate fixed and
¹⁵² moving image pair resulting in a multi-metric registration optimization scenario involving

¹⁵³ 24 image pairs (each label weighted equally) for optimizing correspondence between
¹⁵⁴ neighboring atlases.

¹⁵⁵ **Optimization**

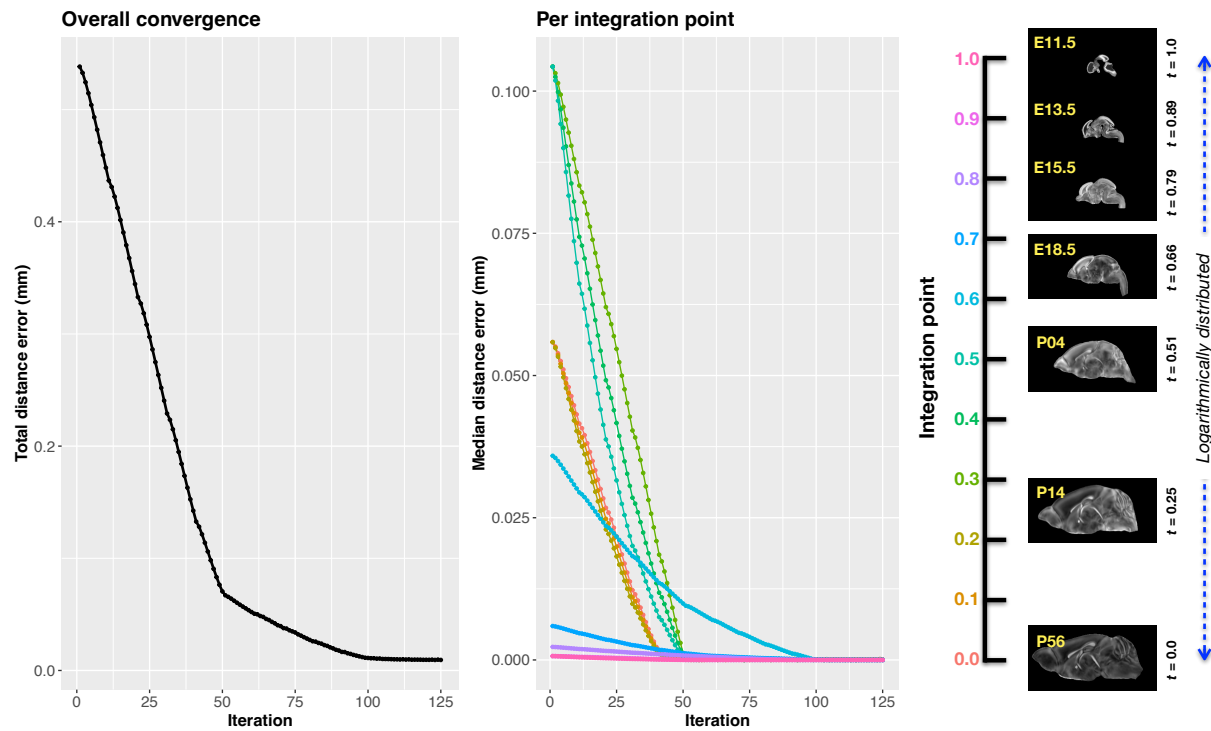


Figure 3: Convergence of the optimization of the velocity field for describing the transformation through the developmental stages from E11.5 through P56.

¹⁵⁶ **Applications**

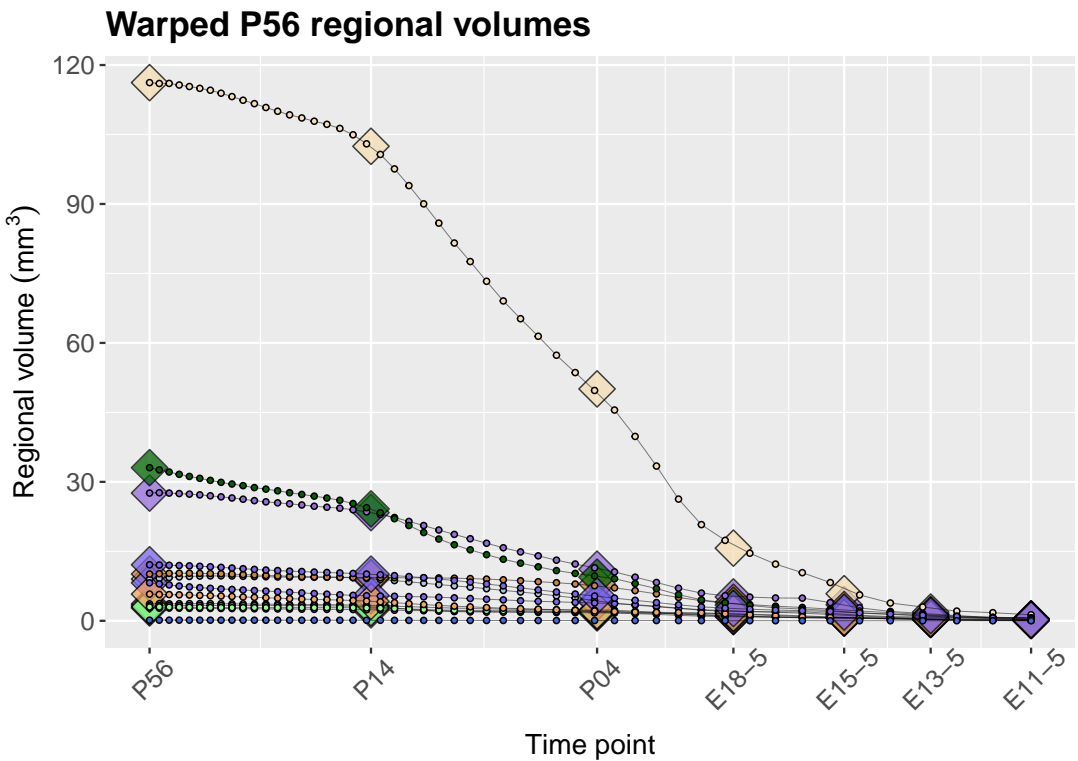


Figure 4: Warped P56.

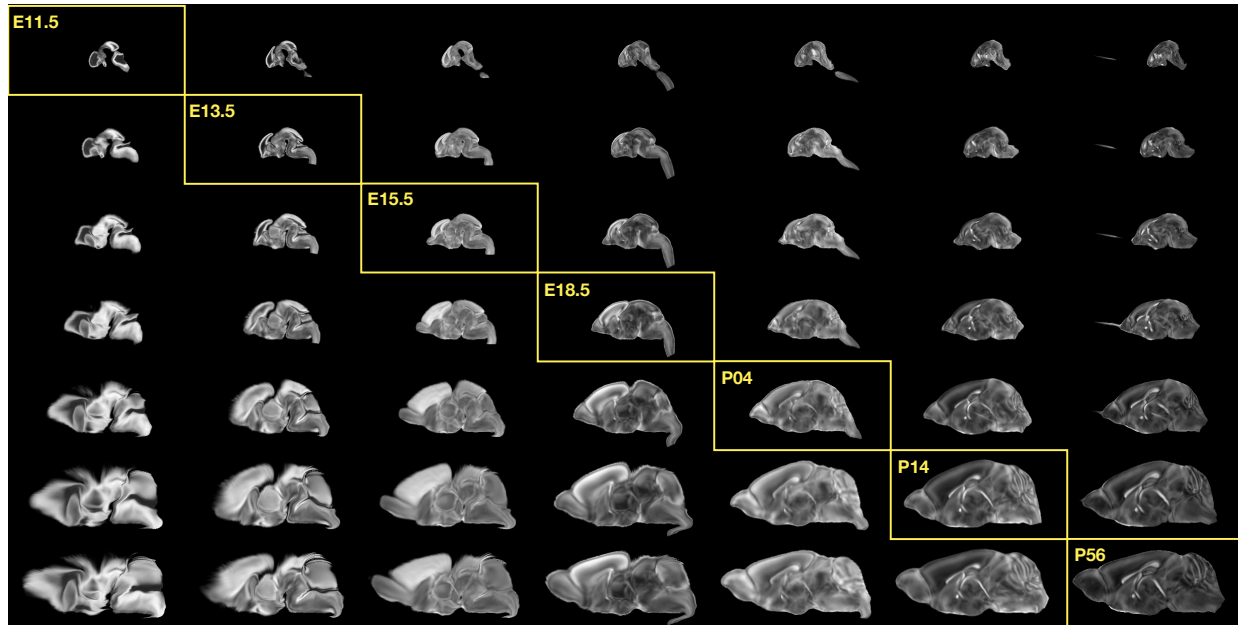


Figure 5: Mid-sagittal visualization of the effects of the transformation model in warping every developmental stage to the time point of every other developmental stage. The original images are located along the diagonal. Columns correspond to the warped original image whereas the rows represent the reference space to which each image is warped.

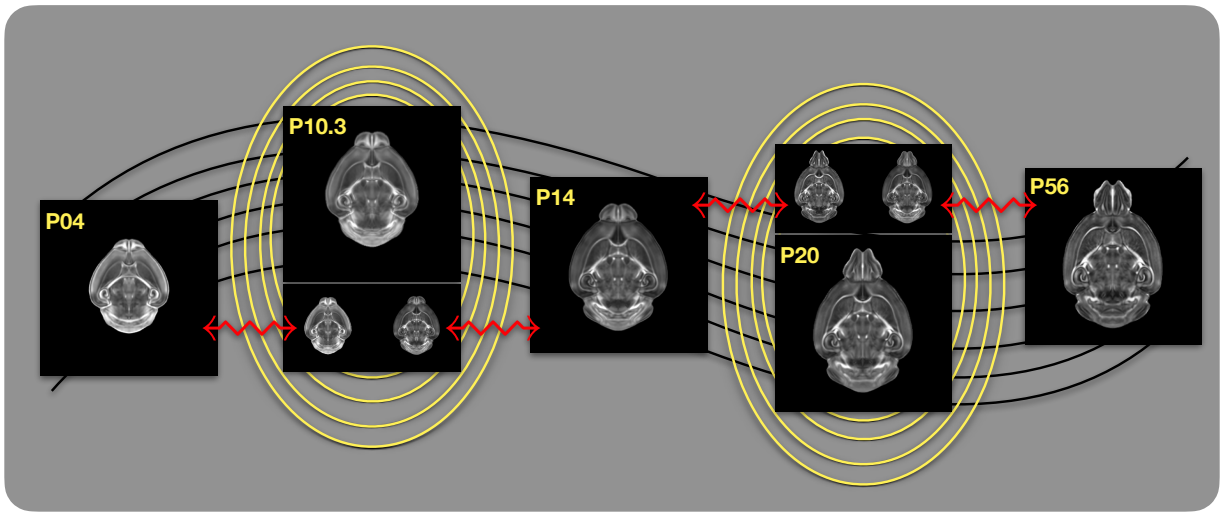


Figure 6: Illustration of the use of the velocity flow model for creating pseudo-templates at continuous time points not represented in one of the existing developmental stages. For example, FA templates at time point P10.3 and P20 can be generated by warping the existing temporally adjacent developmental templates to the target time point and using those images in the ANTsX template building process.

¹⁵⁷ **Methods**

¹⁵⁸ **Preprocessing: bias field correction and denoising**

¹⁵⁹ As in human studies, bias field correction and image denoising are standard preprocessing
¹⁶⁰ steps in improving overall image quality in mouse brain images. The bias field, a gradual
¹⁶¹ spatial intensity variation in images, can arise from various sources such as magnetic field in-
¹⁶² homogeneity or acquisition artifacts, leading to distortions that can compromise the quality
¹⁶³ of brain images. Correcting for bias fields ensures a more uniform and consistent representa-
¹⁶⁴ tion of brain structures, enabling accurate quantitative analysis. Additionally, brain images
¹⁶⁵ are often susceptible to various forms of noise, which can obscure subtle features and affect
¹⁶⁶ the precision of measurements. Denoising techniques help mitigate the impact of noise, en-
¹⁶⁷ hancing the signal-to-noise ratio and improving the overall image quality. The well-known
¹⁶⁸ N4 bias field correction algorithm²⁴ has its origins in the ANTs toolkit which was imple-
¹⁶⁹ mented and introduced into the ITK toolkit. Similarly, ANTsX contains an implementation
¹⁷⁰ of a well-performing patch-based denoising technique⁵³ and is also available as a image filter
¹⁷¹ to the ITK community.

¹⁷² **ANTsXNet mouse brain applications**

¹⁷³ *General notes regarding deep learning training.*

¹⁷⁴ All network-based approaches described below were implemented and organized in the
¹⁷⁵ ANTsXNet libraries comprising Python (ANTsPyNet) and R (ANTsRNet) analogs using the
¹⁷⁶ Keras/Tensorflow libraries available as open-source in ANTsX GitHub repositories. For the
¹⁷⁷ various applications, both share the identically trained weights for mutual reproducibility.
¹⁷⁸ Training data was provided by manual labeling by various co-authors and expanded using
¹⁷⁹ both intensity-based and shape-based data augmentation techniques.

¹⁸⁰ Intensity-based data augmentation consisted of randomly added noise based on ITK
¹⁸¹ functionality, simulated bias fields based on N4 bias field modeling, and histogram
¹⁸² warping for mimicking well-known MRI intensity nonlinearities.^{25,54} These augmentation

183 techniques are available in ANTsXNet (only ANTsPyNet versions are listed): simulated
184 bias field: `simulate_bias_field(...)`, image noise: `add_noise_to_image(...)`, and
185 MRI intensity nonlinear characterization: `histogram_warp_image_intensities(...)`.
186 Shape-based data augmentation used both random linear and nonlinear deformations. This
187 functionality is also instantiated within ANTsXNet in terms of random spatial warping:
188 `randomly_transform_image_data(...)`.

189 For all GPU training, we used Python scripts for creating custom batch generators. As such
190 batch generators tend to be application-specific, we store them in a separate GitHub reposi-
191 tory for public availability (<https://github.com/ntustison/ANTsXNetTraining>). In terms of
192 GPU hardware, all training was done on a DGX (GPUs: 4X Tesla V100, system memory:
193 256 GB LRDIMM DDR4).

194 *Brain extraction.*

195 Similar to human neuroimage processing, brain extraction is a crucial preprocessing step for
196 accurate brain mapping. Within ANTsXNet, we have created several deep learning networks
197 for brain extraction for several image modalities (e.g., T1, FLAIR, fractional anisotropy).
198 Similarly, for the developmental brain atlas work⁴⁷ we developed similar functionality for
199 mouse brains of different modalities and developmental age. All networks use a conventional
200 2-D U-net architecture⁵⁵ and perform prediction in a slice-wise fashion given the limitations of
201 the acquisition protocols (e.g., missing slices, slice thickness). Currently, coronal and sagittal
202 networks are available for both E13.5 and E15.5 data and coronal network for T2-weighted
203 MRI. In ANTsPyNet, this functionality is available in the program `brain_extraction(...)`.
204 Even when physical brain extraction is performed prior to image acquisition, artifacts, such
205 as bubbles or debris, can complicate subsequent processing. Similar to the brain extraction
206 networks, a 2-D U-net architecture⁵⁵ was created to separate the background and foreground.

207 *Miscellaneous networks: Super-resolution, cerebellum, and hemispherical masking.*

208 To further enhance the data prior to designing mapping protocols, additional networks were
209 created. A well-performing deep back projection network⁵⁶ was ported to ANTsXNet and
210 expanded to 3-D for various super-resolution applications,⁵⁷ including mouse data. Finally,
211 features of anatomical significance, namely the cerebellum and hemispherical midline were

212 captured in these data using deep learning networks.

213 **Image registration**

214 **Intra-slice image registration with missing slice imputation**

215 Volumetric gene expression slice data was collated into 3-D volumes using . . . (ask Jeff).

216 Prior to mapping this volume to the corresponding structural data and, potentially, to the
217 appropriate template, alignment was improved using deformable registration on contiguous
218 slices. However, one of the complications associated with these image data was the un-

219 known number of missing slices, the number of consecutive missing slices, and the different

220 locations of these missing slices. To handle this missing data problem, we found that data
221 interpolation using the B-spline approximation algorithm cited earlier⁵² (ANTsPy function:

222 `fit_bspline_object_to_scattered_data(...)`). This provided sufficient data interpo-
223 lation fidelity to perform continuous slicewise registration. Other possible variants that
224 were considered but deemed unnecessary was performing more than one iteration cycling
225 through data interpolation and slicewise alignment. The other possibility was incorporating
226 the super-resolution technique described earlier. But again, our data did not require these
227 additional steps.

228 **Template generation**

229 ANTsX provides functionality for constructing templates from a set (or multi-modal sets) of
230 input images as originally described⁵⁰ and recently used to create the DevCCF templates.⁴⁷

231 An initial template estimate is constructed from an existing subject image or a voxelwise
232 average derived from a rigid pre-alignment of the image population. Pairwise registration
233 between each subject and the current template estimate is performed using the Symmetric
234 Normalization (SyN) algorithm.³⁹ The template estimate is updated by warping all subjects
235 to the space of the template, performing a voxelwise average, and then performing a “shape
236 update” of this latter image by warping it by the average inverse deformation, thus yielding

²³⁷ a mean image of the population in terms of both the intensity and shape.

²³⁸ **Continuous developmental velocity flow transformation model**

²³⁹ Given multiple, linearly or non-linearly ordered point sets where individual points across
²⁴⁰ are in one-to-one correspondence, we developed an approach for generating a velocity flow
²⁴¹ transformation model to describe a time-varying diffeomorphic mapping as a variant of the
²⁴² inexact landmark matching solution of Joshi and Miller.⁴⁸ Integration of the resulting velocity
²⁴³ field can then be used to describe the displacement between any two time points within this
²⁴⁴ time-parameterized domain. Regularization of the sparse correspondence between point sets
²⁴⁵ is performed using a generalized B-spline scattered data approximation technique,⁵² also
²⁴⁶ developed by the ANTsX developers and contributed to ITK.

²⁴⁷ To apply this methodology to the developmental templates,⁴⁷ we coalesced the manual par-
²⁴⁸ cellations of the developmental templates into 26 common anatomical regions (13 per hemi-
²⁴⁹ sphere). We then used these regions to generate invertible transformations between suc-
²⁵⁰ cessive time points. Specifically each label was used to create a pair of single region images
²⁵¹ resulting in 26 pairs of “source” and “target” images. The multiple image pairs were used
²⁵² to iteratively estimate a diffeomorphic pairwise transform. Given the seven atlases E11.5,
²⁵³ E13.5, E15.5, E18.5, P4, P14, and P56, this resulted in 6 sets of transforms between suc-
²⁵⁴ cessive time points. Given the relative sizes between atlases, on the order of 10^6 points were
²⁵⁵ randomly sampled labelwise in the P56 template space and propagated to each successive
²⁵⁶ atlas providing the point sets for constructing the velocity flow model. Approximately 200
²⁵⁷ iterations resulted in a steady convergence based on the average Euclidean norm between
²⁵⁸ transformed point sets. Ten integration points were used and point sets were distributed
²⁵⁹ along the temporal dimension using a log transform for a more evenly spaced sampling.
²⁶⁰ Further details including links to data and scripts to reproduce our reported results is found
²⁶¹ in the associated GitHub repository.¹

²⁶² One potential application is the possible construction of “pseudo”-templates at currently
²⁶³ non-existing developmental stages.

¹<https://github.com/ntustison/MouseBrainVelocityFlow/>

264 **Visualization**

265 To complement the well-known visualization capabilities of R and Python, e.g., `ggplot2`
266 and `matplotlib`, respectively, image-specific visualization capabilities are available in the
267 `ants.plot(...)` (Python) and `plot.antsImage(...)` (R). These are capable of illustrating
268 multiple slices in different orientations with both other image overlays as well as label images.

269 **References**

- 270 1. Keller, P. J. & Ahrens, M. B. Visualizing whole-brain activity and development at
271 the single-cell level using light-sheet microscopy. *Neuron* **85**, 462–83 (2015).
- 272 2. La Manno, G. *et al.* Molecular architecture of the developing mouse brain. *Nature*
273 **596**, 92–96 (2021).
- 274 3. Wen, L. *et al.* Single-cell technologies: From research to application. *Innovation*
275 (*Camb*) **3**, 100342 (2022).
- 276 4. Oh, S. W. *et al.* A mesoscale connectome of the mouse brain. *Nature* **508**, 207–14
277 (2014).
- 278 5. Gong, H. *et al.* Continuously tracing brain-wide long-distance axonal projections in
279 mice at a one-micron voxel resolution. *Neuroimage* **74**, 87–98 (2013).
- 280 6. Li, A. *et al.* Micro-optical sectioning tomography to obtain a high-resolution atlas of
281 the mouse brain. *Science* **330**, 1404–8 (2010).
- 282 7. Ueda, H. R. *et al.* Tissue clearing and its applications in neuroscience. *Nat Rev*
283 *Neurosci* **21**, 61–79 (2020).
- 284 8. Ståhl, P. L. *et al.* Visualization and analysis of gene expression in tissue sections by
285 spatial transcriptomics. *Science* **353**, 78–82 (2016).
- 286 9. Burgess, D. J. Spatial transcriptomics coming of age. *Nat Rev Genet* **20**, 317 (2019).
287
- 288 10. MacKenzie-Graham, A. *et al.* A multimodal, multidimensional atlas of the C57BL/6J
289 mouse brain. *J Anat* **204**, 93–102 (2004).
- 290 11. Mackenzie-Graham, A. J. *et al.* Multimodal, multidimensional models of mouse brain.
291 *Epilepsia* **48 Suppl 4**, 75–81 (2007).
- 292 12. Dong, H. W. *Allen reference atlas. A digital color brain atlas of the C57BL/6J male*
293 *mouse.* (John Wiley; Sons, 2008).

- 294 13. Wang, Q. *et al.* The allen mouse brain common coordinate framework: A 3D reference
295 atlas. *Cell* **181**, 936–953.e20 (2020).
- 296 14. Johnson, G. A. *et al.* Waxholm space: An image-based reference for coordinating
297 mouse brain research. *Neuroimage* **53**, 365–72 (2010).
- 298 15. Oguz, I., Zhang, H., Rumple, A. & Sonka, M. RATS: Rapid automatic tissue segmen-
299 tation in rodent brain MRI. *J Neurosci Methods* **221**, 175–82 (2014).
- 300 16. Sawiak, S. J., Picq, J.-L. & Dhenain, M. Voxel-based morphometry analyses of in
301 vivo MRI in the aging mouse lemur primate. *Front Aging Neurosci* **6**, 82 (2014).
- 302 17. Ashburner, J. SPM: A history. *Neuroimage* **62**, 791–800 (2012).
- 303
- 304 18. Modat, M. *et al.* Fast free-form deformation using graphics processing units. *Comput
305 Methods Programs Biomed* **98**, 278–84 (2010).
- 306 19. Tyson, A. L. *et al.* Accurate determination of marker location within whole-brain
307 microscopy images. *Sci Rep* **12**, 867 (2022).
- 308 20. Pallast, N. *et al.* Processing pipeline for atlas-based imaging data analysis of struc-
309 tural and functional mouse brain MRI (AIDAmri). *Front Neuroinform* **13**, 42 (2019).
- 310 21. Jenkinson, M., Beckmann, C. F., Behrens, T. E. J., Woolrich, M. W. & Smith, S. M.
311 FSL. *Neuroimage* **62**, 782–90 (2012).
- 312 22. Yeh, F.-C., Wedeen, V. J. & Tseng, W.-Y. I. Generalized q-sampling imaging. *IEEE
313 Trans Med Imaging* **29**, 1626–35 (2010).
- 314 23. Jorge Cardoso, M. *et al.* STEPS: Similarity and truth estimation for propagated
315 segmentations and its application to hippocampal segmentation and brain parcelation.
Med Image Anal **17**, 671–84 (2013).
- 316 24. Tustison, N. J. *et al.* N4ITK: Improved N3 bias correction. *IEEE Trans Med Imaging*
317 **29**, 1310–20 (2010).

- 318 25. Tustison, N. J. *et al.* The ANTsX ecosystem for quantitative biological and medical
319 imaging. *Sci Rep* **11**, 9068 (2021).
- 320 26. Goubran, M. *et al.* Multimodal image registration and connectivity analysis for inte-
321 gration of connectomic data from microscopy to MRI. *Nat Commun* **10**, 5504 (2019).
- 322 27. Celestine, M., Nadkarni, N. A., Garin, C. M., Bougacha, S. & Dhenain, M. Sammba-
323 MRI: A library for processing SmAll-MaMmal BrAin MRI data in python. *Front
Neuroinform* **14**, 24 (2020).
- 324 28. Ioanas, H.-I., Marks, M., Zerbi, V., Yanik, M. F. & Rudin, M. An optimized regis-
325 tration workflow and standard geometric space for small animal brain imaging. *Neuro-
image* **241**, 118386 (2021).
- 326 29. Cox, R. W. AFNI: What a long strange trip it's been. *Neuroimage* **62**, 743–7 (2012).
327
- 328 30. Ni, H. *et al.* A robust image registration interface for large volume brain atlas. *Sci
329 Rep* **10**, 2139 (2020).
- 330 31. Jin, M. *et al.* SMART: An open-source extension of WholeBrain for intact mouse
331 brain registration and segmentation. *eNeuro* **9**, (2022).
- 332 32. Fürth, D. *et al.* An interactive framework for whole-brain maps at cellular resolution.
333 *Nat Neurosci* **21**, 139–149 (2018).
- 334 33. Negwer, M. *et al.* FriendlyClearMap: An optimized toolkit for mouse brain mapping
335 and analysis. *Gigascience* **12**, (2022).
- 336 34. Klein, S., Staring, M., Murphy, K., Viergever, M. A. & Pluim, J. P. W. Elastix: A
337 toolbox for intensity-based medical image registration. *IEEE Trans Med Imaging* **29**,
196–205 (2010).
- 338 35. Carey, H. *et al.* DeepSlice: Rapid fully automatic registration of mouse brain imaging
339 to a volumetric atlas. *Nat Commun* **14**, 5884 (2023).

- 340 36. Bajcsy, R. & Broit, C. Matching of deformed images. in *Sixth International Conference on Pattern Recognition (ICPR'82)* 351–353 (1982).
- 341
- 342 37. Bajcsy, R. & Kovacic, S. Multiresolution elastic matching. *Computer Vision, Graphics, and Image Processing* **46**, 1–21 (1989).
- 343
- 344 38. Gee, J., Sundaram, T., Hasegawa, I., Uematsu, H. & Hatabu, H. Characterization of regional pulmonary mechanics from serial magnetic resonance imaging data. *Acad Radiol* **10**, 1147–52 (2003).
- 345
- 346 39. Avants, B. B., Epstein, C. L., Grossman, M. & Gee, J. C. Symmetric diffeomorphic image registration with cross-correlation: Evaluating automated labeling of elderly and neurodegenerative brain. *Med Image Anal* **12**, 26–41 (2008).
- 347
- 348 40. Klein, A. *et al.* Evaluation of 14 nonlinear deformation algorithms applied to human brain MRI registration. *Neuroimage* **46**, 786–802 (2009).
- 349
- 350 41. Murphy, K. *et al.* Evaluation of registration methods on thoracic CT: The EMPIRE10 challenge. *IEEE Trans Med Imaging* **30**, 1901–20 (2011).
- 351
- 352 42. Baheti, B. *et al.* The brain tumor sequence registration challenge: Establishing correspondence between pre-operative and follow-up MRI scans of diffuse glioma patients. (2021).
- 353
- 354 43. Wang, H. *et al.* Multi-atlas segmentation with joint label fusion. *IEEE Trans Pattern Anal Mach Intell* **35**, 611–23 (2013).
- 355
- 356 44. Tustison, N. J. *et al.* Optimal symmetric multimodal templates and concatenated random forests for supervised brain tumor segmentation (simplified) with ANTsR. *Neuroinformatics* (2014) doi:[10.1007/s12021-014-9245-2](https://doi.org/10.1007/s12021-014-9245-2).
- 357
- 358 45. Tustison, N. J., Yang, Y. & Salerno, M. Advanced normalization tools for cardiac motion correction. in *Statistical atlases and computational models of the heart - imaging and modelling challenges* (eds. Camara, O. et al.) vol. 8896 3–12 (Springer International Publishing, 2015).
- 359

- 360 46. McCormick, M., Liu, X., Jomier, J., Marion, C. & Ibanez, L. ITK: Enabling repro-
361
362 47. Kronman, F. A. *et al.* Developmental mouse brain common coordinate framework.
363 *bioRxiv* (2023) doi:[10.1101/2023.09.14.557789](https://doi.org/10.1101/2023.09.14.557789).
- 364 48. Joshi, S. C. & Miller, M. I. Landmark matching via large deformation diffeomor-
365
366 49. Christensen, G. E., Rabbitt, R. D. & Miller, M. I. Deformable templates using large
367 deformation kinematics. *IEEE Trans Image Process* **5**, 1435–47 (1996).
- 368 50. Avants, B. B. *et al.* The optimal template effect in hippocampus studies of diseased
369 populations. *Neuroimage* **49**, 2457–66 (2010).
- 370 51. Tustison, N. J. *et al.* Optimal symmetric multimodal templates and concatenated
371 random forests for supervised brain tumor segmentation (simplified) with ANTsR.
Neuroinformatics **13**, 209–25 (2015).
- 372 52. Tustison, N. J. & Amini, A. A. Biventricular myocardial strains via nonrigid regis-
373
374 53. Manjón, J. V., Coupé, P., Martí-Bonmatí, L., Collins, D. L. & Robles, M. Adaptive
375 non-local means denoising of MR images with spatially varying noise levels. *J Magn
Reson Imaging* **31**, 192–203 (2010).
- 376 54. Nyúl, L. G., Udupa, J. K. & Zhang, X. New variants of a method of MRI scale
377 standardization. *IEEE Trans Med Imaging* **19**, 143–50 (2000).
- 378 55. Falk, T. *et al.* U-net: Deep learning for cell counting, detection, and morphometry.
379 *Nat Methods* **16**, 67–70 (2019).
- 380 56. Haris, M., Shakhnarovich, G. & Ukita, N. Deep back-projection networks for super-
381 resolution. in *2018 IEEE/CVF Conference on Computer Vision and Pattern Recog-
nition* 1664–1673 (2018). doi:[10.1109/CVPR.2018.00179](https://doi.org/10.1109/CVPR.2018.00179).

- ³⁸² 57. avants, brian *et al.* Concurrent 3D super resolution on intensity and segmentation
³⁸³ maps improves detection of structural effects in neurodegenerative disease. *medRxiv*
(2023) doi:[10.1101/2023.02.02.23285376](https://doi.org/10.1101/2023.02.02.23285376).